RESEARCH METHODS

Multiplexed whole-animal imaging with reversibly switchable optoacoustic proteins

Kanuj Mishra[1], Mariia Stankevych[1], Juan Pablo Fuenzalida-Werner[1], Simon Grassmann[2], Vipul Gujrati[1,3], Yuanhui Huang[1,3], Uwe Klemm[1], Veit R. Buchholz[2], Vasilis Ntziachristos[1,3], Andre C. Stiel[1]*

We introduce two photochromic proteins for cell-specific in vivo optoacoustic (OA) imaging with signal unmixing in the temporal domain. We show highly sensitive, multiplexed visualization of T lymphocytes, bacteria, and tumors in the mouse body and brain. We developed machine learning–based software for commercial imaging systems for temporal unmixed OA imaging, enabling its routine use in life sciences.

INTRODUCTION

Photo- or optoacoustic (OA) imaging combines optical contrast with ultrasound resolution, enabling high-resolution, real-time in vivo imaging well beyond the 1-mm penetration depth typical of microscopy methods (*1*, *2*). OA has already provided intriguing insights into tumor heterogeneity (*3*), neuronal dynamics (*4*), psoriasis (*5*), and brown fat metabolism (*6*) based on endogenous contrast from hemoglobin and lipids (*7*, *8*). This is complemented by theranostic research (*9*, *10*) and clinical application (*11*), e.g., imaging of Crohn's disease (*12*). However, OA imaging has not yet become a routine tool in life sciences because of the lack of strong OA contrast agents that can be expressed in desired cell types (*13*). The few transgenic labels used in OA so far (*8*) give weak signals that cannot rise above the strong background due to hemoglobin. Photochromic proteins that can be reversibly switched between two states by light can overcome this limitation by entirely separating the label signal, which modulates in accordance with the illumination, from the background, which remains constant (*14*). This concept, despite being validated in several studies (*15*–*20*), has not been implemented widely because it requires complex instrumentation and data analysis tools. Here, we introduce two reversibly switchable OA proteins (rsOAPs) and demonstrate their use with widely accessible off-the-shelf commercial imaging systems as well as our open-access machine learning (ML)–based software code for analysis. One of our new rsOAPs shows high switching speeds and dynamic range of photomodulation that allow us to resolve the signals of different cell populations labeled with differentiable rsOAPs in close proximity in the same animal, demonstrating the potential for simultaneous tracking of different cellular processes through temporal multiplexing.

RESULTS

Engineering of rsOAPs

Bacterial photoreceptors called bacteriophytochromes (BphPs) (*21*) have emerged as most suitable for rsOAP development due to their strong absorption in the near-infrared range and low photofatigue (*22*). To identify the most promising candidate for further development, we screened eight native BphPs (table S1) and selected the one from *Rhizobium etli*. A set of truncations enabled us to minimize its size and optimize its photoswitching characteristics. In brief, on the basis of existing structural data as well as homology models, we created truncations containing the minimum PAS-GAF-PHY photosensory core domains [photosensory core module (PCM)] together with extra amino acids from the annotated linkers between PHY and histidine kinase domains and tested their characteristics in regard to signal generation and photoswitching (Fig. 1, A to E,

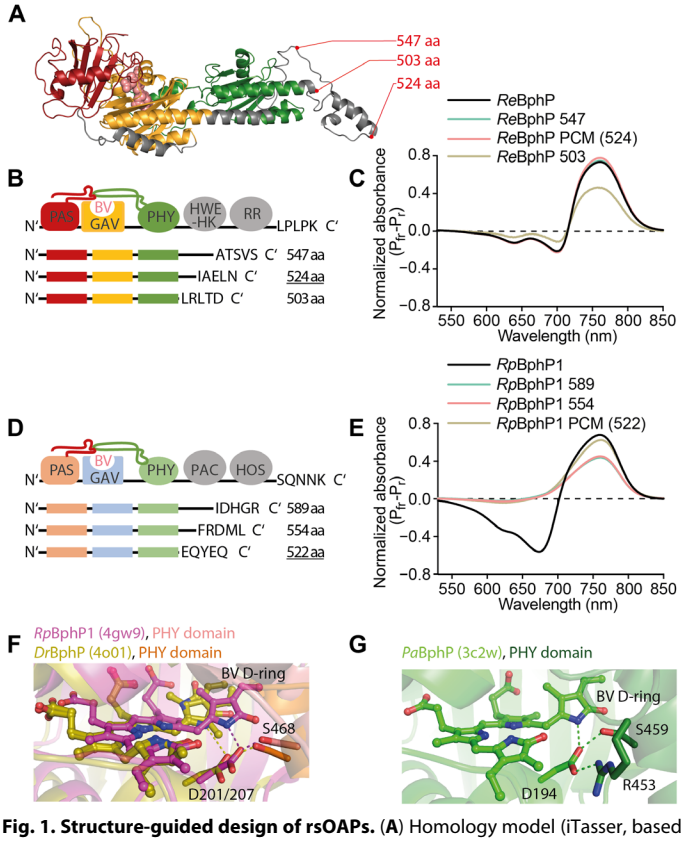

Fig. 1. Structure-guided design of rsOAPs. (**A**) Homology model (iTasser, based on 6g1y) of *Re*BphP-PCM. Truncation sides indicated. (**B**) Schematic representation of truncations. (**C**) Photoinduced differential spectra for truncations. (**D** and **E**) Similar representations for *Rp*BphP1. (**F**) Stabilization of the BV D-ring in *Rp*BphP1 and *Dr*BphP. (**G**) Similar representation for PaBphP, which shows an arginine similar to *Re*BphP, presumably abstracting D194 and destabilizing the P_{fr} state, yielding a faster photoswitching.

[1]Institute of Biological and Medical Imaging (IBMI), Helmholtz Zentrum München, Neuherberg, Germany. [2]Institute for Medical Microbiology, Immunology and Hygiene, Technische Universität München (TUM), Munich, Germany. [3]Chair of Biological Imaging and Center for Translational Cancer Research (TranslaTUM), Technische Universität München (TUM), Munich, Germany.
*Corresponding author. Email: andre.stiel@helmholtz-muenchen.de

and note S1). The final variant *Re*BphP-PCM shows twofold larger change in OA signal (Fig. 2G), more than fivefold faster switching (Fig. 2, C and D), and greater resistance to photofatigue than other rsOAPs (Fig. 2E), while its high molar absorbance is on par with the recently described *Deinococcus radiodurans Dr*BphP-PCM (92,000 M^{-1} cm^{-1}; Fig. 2, B and G) (*19*). Those characteristics enable higher numbers of switching cycles per second, which improves sensitivity and allows imaging over longer timeframes. On the molecular level, this acceleration of switching speed is the result of a less stabilized P_{fr} state favoring the photoinduced transition to P_r. The destabilization is likely caused by an arginine present in *Re*BphP but not in *Rp*BphP1 and *Dr*BphP. This arginine, by interacting with a conserved aspartate, which, in turn, interacts with the D-ring of the P_{fr} state chromophore, weakens P_{fr} stabilization (Fig. 1, F and G, and note S1).

Our truncation strategy also proved successful in obtaining a switchable *Rp*BphP1-PCM from *Rhodopseudomonas palustris*, in contrast to a previous report that truncated forms of this protein do not undergo reversible switching (*19*). Our engineered *Rp*BphP1-PCM maintains the far-red state (P_{fr}) extinction coefficient and photochromic behavior of the parental *Rp*BphP1 (Figs. 1E and 2B and fig. S1), and the change in its OA signal following illumination at 770 nm is similar to that of the previously described *Dr*BphP-PCM (Fig. 2G). (Plasmid for expressing *Re*BphP-PCM in bacteria and eukaryotic cells or for introduction into viral vectors can be obtained from Addgene.) Both new rsOAPs are monomeric (fig. S2) and show higher expression in mammalian cells than the full-length parental proteins (fig. S3). The two developed rsOAPs and *Dr*BphP-PCM show distinctive switching speeds, which is the reason for our ability to discriminate the proteins in vivo successfully. As a result, probes expressed in different cells in close proximity in the animal can be distinguished during high-resolution OA imaging.

OA imaging using ML-based temporal unmixing

We performed all OA imaging using an off-the-shelf, commercially available multispectral OA tomography device with a 10-Hz pulsed tunable laser and a 256-element transducer array (MSOT, iThera Medical). Off-switching of rsOAPs was achieved with light at 770 nm, which gave the highest difference in OA signal intensity between the "on" and "off" states (fig. S5A), while on switching was achieved using light at 680 nm. Lower wavelengths did not substantially improve the transition to the on state (fig. S5B). The number of laser pulses per wavelength was chosen to cover the full switching kinetics, but it can be significantly reduced using information-content analysis, which allows an estimate of the minimal number of cycles and pulses per cycle required to discern the labeled structure, thus effectively limiting imaging dwell time, which is essential for, e.g., time-resolved studies (Fig. 2H, fig. S6, and note S2). All temporal unmixing was conducted with in-house code developed to analyze time-varying patterns in the reconstructed data in the frequency and time domains using classic ML approaches (Fig. 3, Materials and Methods, and notes S3 and S4). In brief, after running fluence and motion correction on the data, a range of distinctive features

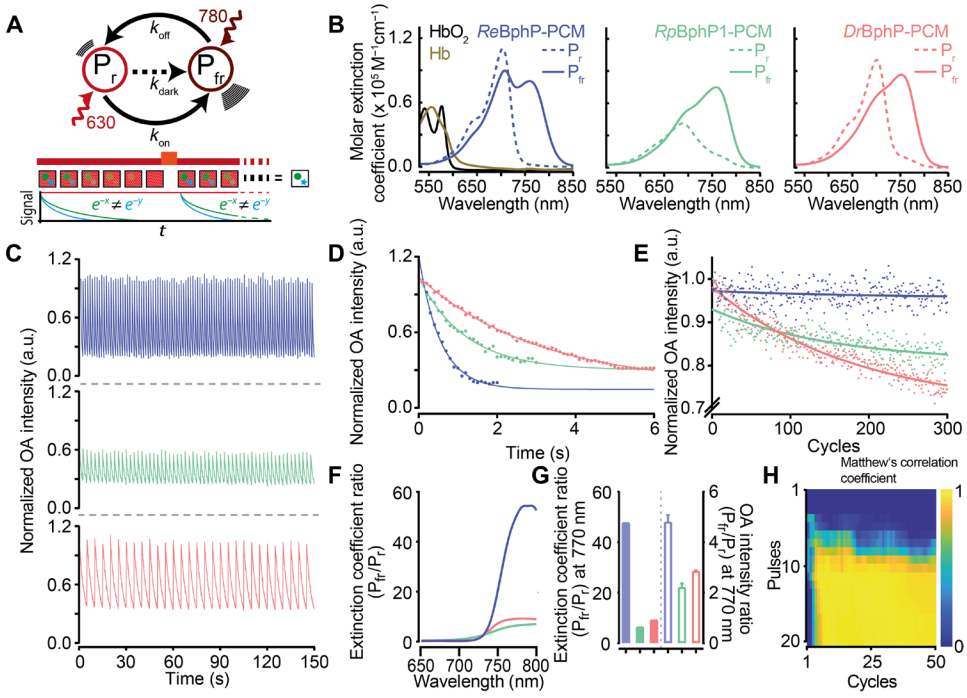

Fig. 2. In vitro characterization of *Re*BphP-PCM and *Rp*BphP1-PCM in comparison to *Dr*BphP-PCM. (**A**) Principle of photoswitching in BphPs (top) and concept of temporal unmixing of two labels (green ball and blue star; bottom). Illumination shown in dark red (780 nm) and red (630 nm). P_r refers to the red state, while P_{fr} refers to the far-red state. The bottom part of the panel was adapted with permission from (*14*). (**B**) Absorbance spectra of P_r and P_{fr} states of the three rsOAPs in comparison to hemoglobin (HbO_2 and Hb, 1999, S. Prahl, omlc.org). (**C**) Switching cycles of the rsOAPs. Only OA signal at 770 nm is shown. a.u., arbitrary units. (**D**) Single switching cycle from (C), shown with an exponential fit. (**E**) Photofatigue of the proteins per cycle. (**F**) Absorbance ratio between the P_{fr} and P_r state for different wavelengths. (**G**) Absorbance (filled bars) and OA signal intensity (hollow) ratio between the P_{fr} and P_r state for the three rsOAPs at 770 nm. (**H**) Matthew's coefficient shown as a function of number of cycles and pulses. Shown is the analysis of a 4T1 tumor expressing *Re*BphP-PCM; histology was used as ground truth. All proteins have been adjusted to equal Soret peak absorption.

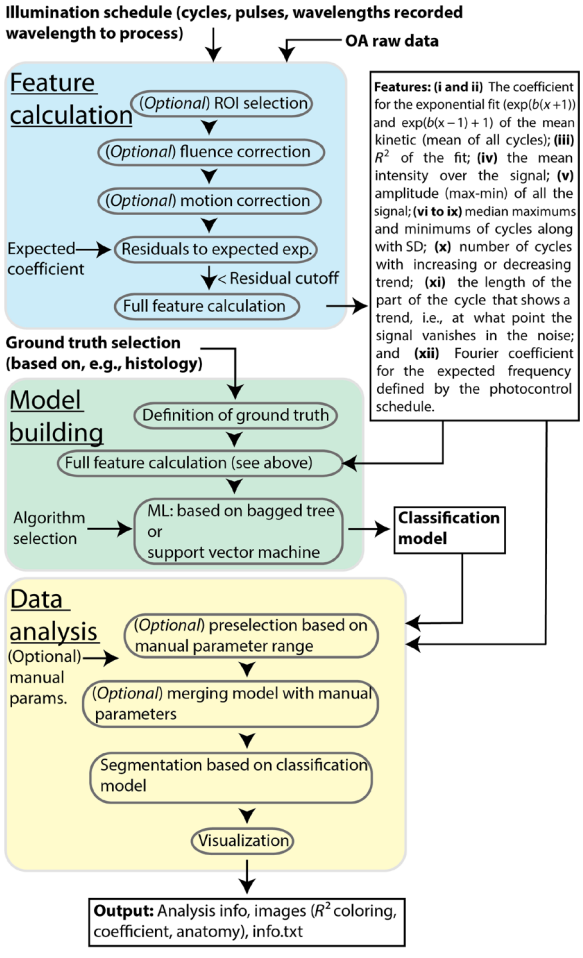

Fig. 3. Schematic flow of the ML-based analysis strategy and main scripts. The time-varying patterns in the OA raw data are extracted in the "Feature calculation" (blue) and analyzed using a classification model in the "Data analysis" step (yellow). In "Model building" (green), a classification model is trained based on imaging data with associated histology ground truth. In the script, two algorithms can be selected: bagged tree or support vector machine. For uniformity, the images shown in this work exclusively use the bagged tree approach, although the support vector machine has some virtues (note S4).

was extracted from the photomodulated signal for each voxel of the tomography images. On the basis of a set of these data and corresponding histology as ground truth, a bagged random forest algorithm (*23*) was trained and validated on independent datasets of a different type to prevent overfitting. The ensuing model was then used to analyze all data in this study. The code for data preparation, for analysis with the model used in this work, and for generation of new models is available to the community along with graphical user interfaces.

The OA imaging scheme is shown in Fig. 4A. First, we used rsOAPs for superficial in vivo imaging. We imaged the development of 4T1 mouse mammary gland tumors coexpressing *Re*BphP-PCM and green fluorescent protein (GFP) after they were grafted onto the backs of FoxN1 nude mice ($n = 3$). The initial population of 0.8×10^6 injected cells was readily visualized separate from all background absorbers (Fig. 4B), as was the growing tumor mass at all days after injection (fig. S7, A to D). To test whether this imaging is also possible in brain tissue after light passes through the skull, we implanted 0.7×10^6 4T1 cells coexpressing *Re*BphP-PCM and GFP at a depth of 3.6 mm and imaged them immediately thereafter. Comparison of the OA images with fluorescence images obtained after sacrificing mice revealed perfect overlap of the labeling, confirming background-free identification of 1.4×10^5 cells deep in the mouse brain (Fig. 4C). Next, we used the same rsOAP to image deep-seated tumors of HCT116 human colon carcinoma cells implanted intraperitoneally ($n = 2$). From day 3 onward, we were able to visualize the growth of several individual tumor sites to a depth of ~1 cm (fig. S7, E and F). Comparison of OA images and histology obtained after sacrifice confirmed identification of all malignant tissue (Fig. 4, D to F, and fig. S7, E and G), including small tumors or metastatic patches containing less than 10,000 cells (fig. S7, I and J).

To assess the sensitivity of imaging with our rsOAPs, we imaged dorsal implants of Matrigel containing different numbers of Jurkat T lymphocytes stably coexpressing *Re*BphP-PCM and GFP in mice (Fig. 4G). We detected populations as small as 500 cells/μl, suggesting the potential for sensitive tracking of immune processes. Similarly, imaging of dorsal implants of Matrigel containing bacteria expressing *Re*BphP-PCM detected populations as small as 14,000 bacteria/μl (Fig. 4H). This sensitivity may be useful for studying and optimizing bacteria-based tumor therapies (*24*).

A strong advantage of photocontrollable labels is the possibility to delineate multiple labels based on their individual switching kinetics. To demonstrate this, we imaged 1-mm alginate beads filled with *Escherichia coli* expressing *Re*BphP-PCM, *Rp*BphP1-PCM, or *Dr*BphP-PCM. All beads were unambiguously identified on the basis of their switching kinetics (Fig. 5A). The same differentiation was achieved in vivo after implanting Jurkat T lymphocytes expressing *Re*BphP-PCM or *Dr*BphP1-PCM and *E. coli* expressing *Rp*BphP1-PCM into the back of mice (Fig. 5B).

Because the kinetics of photoswitching are energy dependent, fluence changes due to light attenuation by surrounding absorbers—photochromic or static—complicates temporal multiplexing (note S5). Thus, one aim of our development of the fast-switching *Re*BphP-PCM was to achieve a switching time constant clearly separate from other rsOAPs. We show that 4T1 tumor expressing *Re*BphP-PCM and GFP are readily distinguished from infiltrating *Dr*BphP-PCM–expressing *E. coli* cells (intratumorally injected 10^8 bacteria; Fig. 5, D and E). This means that multiplexing is possible for co-registration studies and that the concentrations of the labels can be estimated based on the convoluted kinetics (fig. S8). Similarly, we show this for two populations of rsOAP labeled Jurkat T lymphocytes in a 4T1 tumor (intratumorally injected 5×10^5 cells; Fig. 5C). Hence, temporally unmixed multiplexed OA imaging of cells of the immune system enables following their function and involvement in disease mechanism in vivo, longitudinal on the organism level.

DISCUSSION

The combination of OA and transgenic rsOAP labels allows the tracking of specific cell populations in vivo, which can open up possibilities for longitudinal studies of intact animals in diverse fields such as immunology, developmental biology, neurology, and cancer research. To support these studies, we describe next-generation rsOAPs that provide faster switching and greater resistance to photofatigue than existing rsOAPs, allowing highly sensitive detection, and importantly true multiplexing, without interference from hemoglobin or other abundant absorbers in vivo. These rsOAPs can be used with

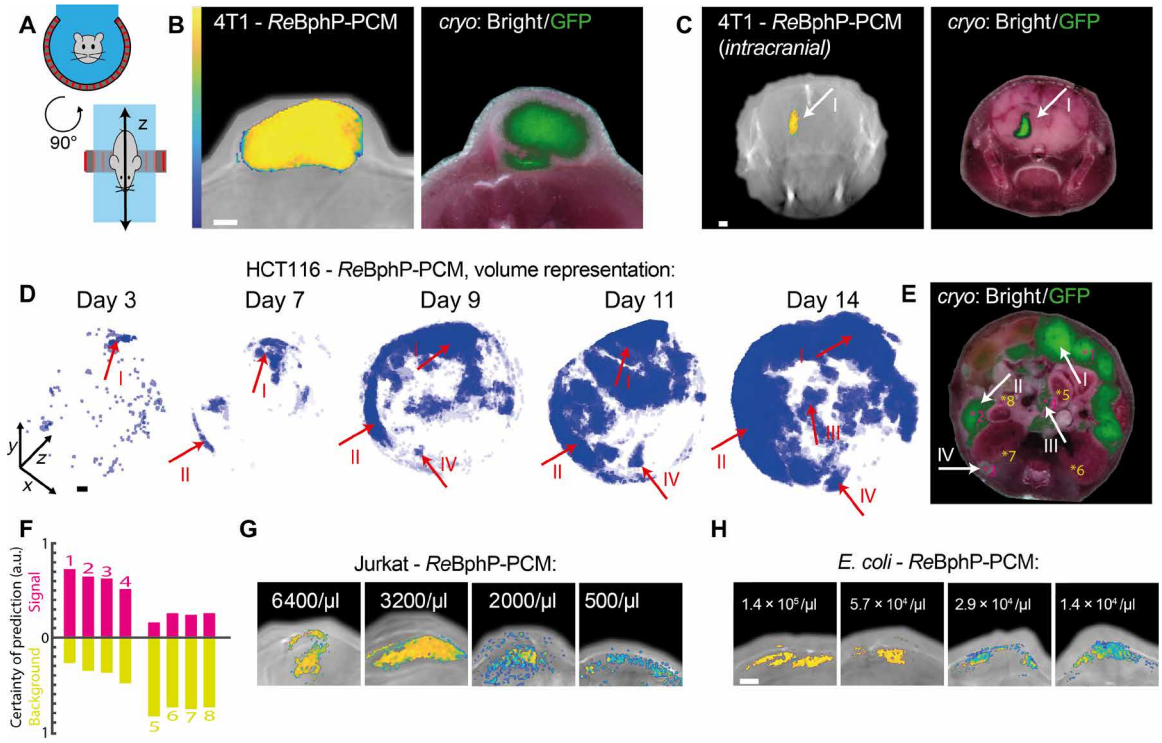

Fig. 4. MSOT imaging of *Re*BphP-PCM and other rsOAPs. In certain experiments, GFP was coexpressed to allow fluorescence imaging of histology slices. (**A**) Schematic of OA tomography used in this work. (**B**) 4T1 cells (0.8×10^6 injected subcutaneously) stably expressing *Re*BphP-PCM and imaged on day 9. (**C**) 4T1 cells (0.7×10^6 injected intracranially) stably expressing *Re*BphP-PCM imaged at a depth of 3.6 mm in the brain (arrow I) immediately after injection. (**D**) Volume representation of HCT116 cells (1.5×10^6 injected intraperitoneally) stably expressing *Re*BphP-PCM at consecutive time points. (**E**) Histology of the same mouse at day 14. (D and E) Arrows indicate distinctive tumor masses. (**F**) Certainty of prediction (weighted sum of tree scores) indicating quality of discerning label signal or background of regions of interest shown in (E) (right). (**G**) Imaging of the indicated concentrations of Jurkat T cells in Matrigel expressing *Re*BphP-PCM immediately after subcutaneous implantation; because of the polymerization process, no homogeneity is expected. (**H**) Imaging of the indicated concentrations of *E. coli* expressing *Re*BphP-PCM in Matrigel immediately after subcutaneous implantation. In (B), (C), (G), and (H), color maps refer to R^2 (detection quality). All slices are single representative slices. All scale bars, 1 mm. Earlier time points and data from additional mice can be found in fig. S7.

off-the-shelf equipment and our ML-based open-access image processing code to detect populations of fewer than 500 cells in vivo. The approach relies entirely on a time series of images, thus making the concept translatable between different OA imaging devices. These tools will facilitate the wider use of OA imaging in life sciences, particularly for the study of cellular dynamics and interactions on the level of whole organisms.

MATERIALS AND METHODS

Cloning

*Rp*BphP1 (*16*) was obtained from Addgene (V. Verkhusha, plasmid no. 79845). Mammalian optimized *Re*BphP was synthesized as gene strings (GeneArt, Life Technologies, Regensburg, Germany). All other BphPs used in the study have been a gift from A. Möglich (University of Bayreuth, Germany).

For bacterial protein expression, the coding sequences of all BphPs used in the study except *Rp*BphP1 were polymerase chain reaction (PCR)–amplified as a Nde I/Xho I fragment and cloned into the second multiple cloning site of the pET-Duet1 vector (Novagen, Merck Millipore). *Rp*BphP1 was PCR-amplified as a Nde I/Pac I fragment and cloned into the second multiple cloning site of the pET-Duet1 vector. In addition, for biliverdin synthesis, the heme oxygenase (HO) of *Nostoc sp.* was cloned using Nco I/Hind III into the first multiple cloning site of pET-Duet1.

For equimolar mammalian expression, first, *Re*BphP_P2A and mCherry were PCR-amplified and then stitched using overlap PCR as an Eco RI/Xba I fragment and cloned in a pcDNA3.0 vector (Thermo Fisher Scientific). Later similar constructs for other BphPs were made by amplifying them as Eco RI/Not I fragment and inserted in place of *Re*BphP1-PCM in the above construct. The resulting plasmids allowed the equimolar coexpression of *Rp*BphP1, *Rp*BphP1-PCM, *Re*BphP-PCM, *Re*BphP-PCM, or *Dr*BphP-PCM and mCherry proteins.

Protein expression and purification

Proteins have been expressed in *E. coli* strain BL21 (DE3) (New England Biolabs, #C2527). In brief, plasmids expressing BphPs and HO were transformed into the BL21 host cells. Bacterial cells were grown in LB media supplemented with ampicillin at 37°C until the culture reached OD (optical density) 0.6, followed by induction of protein expression by addition of IPTG (isopropyl-β-D-thiogalactopyranoside) and further incubation for 16 to 18 hours at 22°C. The next day, the bacterial pellet was collected by centrifugation and pellet was resuspended in phosphate-buffered saline (PBS). After cell lysis, proteins were purified by immobilized metal affinity chromatography in PBS,

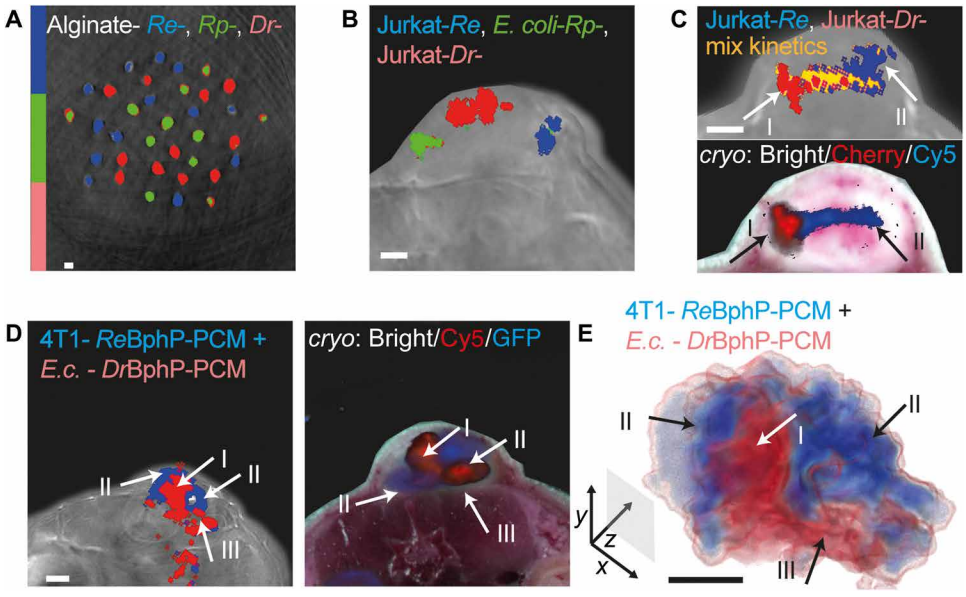

Fig. 5. Parallel visualization of multiple rsOAPs in MSOT. (**A**) Imaging of an alginate bead phantom containing *E. coli* expressing rsOAPs *Re*BphP-PCM, *Rp*BphP1-PCM, and *Dr*BphP-PCM. (**B**) Imaging of Jurkat T cells and *E. coli* (1.4×10^6) expressing each of the three rsOAPs imaged immediately after implantation into a 4T1 tumor. (**C**) Imaging of a 4T1 tumor with implants of two Jurkat T cells expressing rsOAPs. Zones of mixture of the two populations with distinct kinetics are colored yellow. In (A) to (E), color maps indicate clusters showing distinguishable kinetics. (**D**) Imaging of a 4T1 tumor stably expressing *Re*BphP-PCM at day 9 (arrows II and III) imaged immediately after *E. coli* (10^8 cells) expressing *Dr*BphP-PCM have been injected into the tumor (arrow I). Histology confirmation is inferred from fluorescence in *Dr*BphP-PCM (Cy5 only) and *Re*BphP-PCM (GFP primarily). (**E**) Volume representation of *k*. All slices are single representative slices. All scale bars, 1 mm.

followed by gel filtration on a HiLoad 26/600 Superdex 75 pg (GE Healthcare Life Sciences, Freiburg, Germany).

Absorption and fluorescence spectroscopy

For absorption spectra, the purification buffer was exchanged against PBS and the proteins were measured with a Shimadzu UV-1800 spectrophotometer (Shimadzu Inc., Kyoto, Japan) using a 100-µl quartz cuvette. To measure the ON (P_{fr}) and OFF (P_r) spectra of respective proteins, photoswitching was carried out using 650/20-nm or 780/20-nm light-emitting diodes (Thorlabs) placed above the quartz cuvette in the spectrophotometer.

Fluorescence measurements for all BphPs were performed with a Cary Eclipse Fluorescence spectrophotometer (Varian Inc., Australia). Photoswitching was carried out as above. Fluorescence measurement was done by fixing excitation wavelength at 700 nm and emission wavelength at 720 nm. Excitation wavelength and emission slit were set to 5 nm, and the absorbance at the excitation wavelength was always equal to 0.1 to avoid inner filter effects.

Mammalian cell culture

4T1 and Jurkat cells were maintained in RPMI 1640. HeLa and HCT116 cells were maintained in Dulbecco's modified Eagle's medium (DMEM) and McCoy 5A medium, respectively. All media were supplemented with 10% fetal bovine serum (Invitrogen) and antibiotics [penicillin (100 U/ml) and streptomycin (100 mg/ml)]. Cells were cultivated at 37°C and 5% CO_2.

Stable cell lines

Tissue culture

The Platinum-E and RD114 packaging cell lines were cultivated in cDMEM (Complete Dulbecco's modified Eagle medium), HCT116 cell line was grown in McCoy 5A medium (Life Technologies), and 4T1 and Jurkat cells were cultured in cRPMI (Complete Roswell Park Memorial Institute)–1640 Medium. All media were supplemented with 10% fetal calf serum, 0.025% L-glutamine, 0.1% Hepes, 0.001% gentamicin, and 0.002% streptomycin.

Generation of constructs

*Re*BphP-PCM-IRES-GFP was amplified using specific primers (5′-ATTAGCGGCCGCGCCACCATGAGCGGCACCAGAG-3′ and 5′-ATTAGAATTCTCACTTGTACAGCTCGTCCATGCCGTGAGTG-3′) and cloned into the mP71 using Not I and Eco RI restriction sites. The mP71 vector was a gift from W. Uckert.

Generation of cell lines

For retrovirus production, Platinum-E or RD114 packaging cells were transfected with the retroviral vector mP71-*Re*BphP-PCM-IRES-GFP using calcium phosphate precipitation. The supernatant of the packing cells was collected at 48 and 72 hours after transfection and purified from the remaining cells by centrifugation at 1500 rpm at 4°C for 7 min. One day before transduction, non–tissue culture–treated 48-well plates were coated with RetroNectin (Clontech) according to the manufacturer's recommendations overnight at 4°C. After washing once with PBS, virus supernatant was added and centrifuged at 3000*g* and 32°C for 2 hours. Virus supernatant was removed, and cell lines (4T1, HCT116, and Jurkat) were added in 400 µl of the respective medium supplemented with 1:100 LentiBOOST Solution A and 1:100 LentiBOOST Solution B (Sirion Biotech). Cells were then spinoculated at 800*g* at 32°C for 1.5 hours. After 5 days of culture, cells were sorted for high expression of GFP using flow cytometry.

Mouse work

All animal experiments were approved by the government of Upper Bavaria and were carried out in accordance with the approved

guidelines. For 4T1 xenografts of stably expressing *Re*Bphp-PCM and GFP, 0.8×10^6 cells in PBS have been implanted in the back of FoxN1 nude mice (Charles River Laboratories, Boston, USA) and maintained for 9 days. For HCT116 cells expressing *Re*BphP-PCM and GFP, 1.5×10^6 cells in 200 μl PBS have been injected intraperitoneally in FoxN1 nude mice and were maintained for 14 days. For intracranial injections of stably expressing *Re*BphP-PCM and GFP 4T1 cells, mice were first anesthetized according to the animal protocol. The head of the mouse was fixed in a Stereotaxic frame (David Kopf Instruments, model 940), an incision in the skin was made using a scalpel, and a small hole was drilled into the skull. Later, 5-μl cells (0.14×10^6 cells/μl) were injected slowly with a 10-μl Hamilton syringe (26Gs). The incision in the skin was closed using Histoacryl (B. Braun Melsungen AG). The mice were scanned in MSOT and sacrificed immediately after scanning. For Matrigel implants of Jurkat cells expressing *Re*BphP-PCM, different concentrations of cells ranging from 6400 to 500 cells/μl were implanted subcutaneously in the back of the mice. Similarly, bacterial cells expressing *Re*BphP-PCM in different concentrations (1.4×10^5 to 1.4×10^4 cells/μl) were also implanted in the back of the mice. For multiplexing experiment, bacterial cells expressing rsOAPs individually with the concentration of 1.4×10^6 cells/μl were implanted on the back of the mice in the same plane. For multiplexing experiment in vivo, intratumoral injections, bacterial cells expressing *Dr*BphP-PCM resuspended in PBS have been injected into the 4T1 tumor expressing *Re*BphP-PCM and GFP using an insulin syringe with a 30-gauge needle.

For all MSOT imaging, mice have been anesthetized using 2% isoflurane in O_2. Anesthetized mice were placed in the MSOT holder using ultrasound gel and water as coupling media. After termination of the experiments, all mice have been sacrificed and stored at −80°C for cryosectioning.

MSOT setup and data acquisition

Phantom and mice data were acquired using a commercially available MSOT scanner (MSOT In Vision 256-TF, iThera Medical GmbH, Munich, Germany). In brief, nanosecond pulsed light was generated from a tunable optical parametric oscillator (OPO) laser and delivered to the sample through a ring-type fiber bundle. The wavelengths, 680 and 770 nm, were used for photoswitching and imaging in phantoms and in mice. Light absorbed by the sample generates an acoustic signal that propagates through the sample and is detected outside the sample by a cylindrically focused 256-element transducer. The transducer array had a central frequency of 5 MHz (−6 dB was approximately 90%) with a radius of curvature of 40 mm and an angular coverage of 270°. Acoustic signals were detected as time series pressure readouts at 2030 discrete time points at 40 MS/s (Mega-samples per second). The acquired acoustic data were reconstructed using the ViewMSOT version 3.8.1.04 (iThera Medical GmbH, Munich, Germany) software with the following settings: 50 kHz to 6.5 MHz; trim speed of 7.

OA data analysis

All data analysis was conducted using MATLAB2018b. The data reconstructed with ViewMSOT were loaded into MATLAB by iThera MATLAB code (iThera MATLAB, version: msotlib_beta_rev75). All analyses were carried out with the code provided along with this manuscript (note S3). In brief, movement correction was done by phase correlation preliminary to optimization-based image co-registration with the intensity and nonrigid co-registration of frames of the first cycle being used as reference. For further processing, different features of the time series have been computed and are used for classification/switching label detection using an ML model. For fast Fourier transform, repetitive frequency of the whole concatenated signal for each image point is computed to identify signals corresponding to the illumination schedule. For exponential fitting, the normalized mean kinetic of all cycles is used. Then, the coefficients compared to an expected exponential kinetic are calculated and used as a quality measure. Here, positive and negative exponential are considered. Using fit coefficients and quality of fit (R^2) as measures, only 77% accuracy compared to a ground truth is achieved. Thus, additional features are invoked. Overall, all analyzed features are (i and ii) the coefficient for the exponential fit ($\exp(b(x + 1))$ and $\exp(b(x - 1) + 1)$ of the mean kinetic (mean of all cycles); (iii) R^2 of the fit; (iv) the mean intensity over the concatenated signal; (v) max-min of all the data at the pixel; (vi to ix) median maximums and minimums of cycles along with SD; (x) number of cycles with positive or negative trend; (xi) the length of the part of the cycle that shows a trend, i.e., at what point the signal vanishes in the noise; and (xii) Fourier coefficient for the expected frequency defined by the photocontrol schedule. All those are used as predictor values for an unmixing model based on random forest approaches (*23*, *25*)—for overall model, trained on 4T1 day 9 as well as highest concentration of Jurkat T lymphocytes. We used 50 trees in the ensemble, as further increase of number did not lead to out-of-bag error decrease. This approach resulted in model performance increase up to 96% of positive predictive value for ground truth (see note S4 for more details on the use of ML in this work).

For visualization, data were not further processed and are shown against the respective slice at 680 nm as anatomy information, except in the case of 4T1 injected in brain where the anatomy is shown at 900 nm. Representative slices are shown. For clustering, appropriate ranges of the kinetic parameter were chosen on the unmixed data to distinguish different labels.

Cryosectioning

After sacrificing, the mice were cryopreserved at −80°C. To detect the fluorescence in tumors, the respective part of the mouse was embedded in Tissue-Tek O.C.T. (Sakura Finetek Europe B.V., Zoeterwonde, The Netherlands). Sections (10 μm) were cut (Leica CM1950, Leica Microsystems, Wetzlar, Germany) for brain, 4T1, and HCT116 mice at the interval of 150, 250, and 500 μm, respectively, and imaged using a 482/35-nm bandpass for excitation and 535/38-nm bandpass filter for detection of GFP fluorescence. Images were taken using an Andor LucaR charge-coupled device camera (DL-604M, Andor Technology, Belfast, UK) with 10-s exposure and a gain of 10. On the basis of the histology, ground truth on co-registered images was created using a semiautomatic procedure based on anatomical markers and intensity-based multimodal co-registration together with a nonrigid spline-based method and human (two independent)–based selection of signals in the fluorescence images.

Bacterial cell immobilization by entrapment and MSOT imaging

A 2 to 4% (w/v) aqueous solution of sodium alginate was prepared in PBS. *E. coli* strain BL21 cells expressing rsOAPs were harvested by centrifugation (4000 rpm, 20 min) and resuspended in PBS. The cell suspensions were then mixed with sterile alginate. Beads were formed by filling the alginate cell mixtures in the syringe with 30-gauge needle, followed by centrifugation at 300 rpm, which allowed the addition of the mixtures into sterile $CaCl_2$ (200 mM). The cell-containing

beads, 1 mm in diameter, were allowed to solidify for 10 min before $CaCl_2$ was replaced by fresh distilled water. The cell beads were then randomly distributed in the agar phantom with 1.5% (w/w) agar and 3.5% (v/v) intralipid emulsion and imaged in MSOT as described elsewhere.

OA characterization of proteins

For OA characterization of rsOAPs, custom-made experimental setup was used as described earlier (*22*). Briefly, nanosecond excitation pulses were generated by an OPO laser (SpitLight DPSS 250 ZHGOPO, InnoLas) running at a repetition rate of 50 Hz. Constant pulse energy was ensured using a half-wave plate in a motorized rotation stage (PRM1Z8, Thorlabs) and a polarizing beam splitter; using a lookup table and adapting the polarization with the half-wave plate, we kept the power constant at ~1.3 mJ (otherwise mentioned) over the whole illumination schedule. Samples were injected into an acoustically coupled flow chip (μ-Slide I 0.2 Luer, hydrophobic, uncoated, ibidi) and illuminated from one side using a fiber bundle (CeramOptec) at a constant pulse energy of ~1.3 mJ at the fiber output. Photoswitching was carried out by illuminating the sample alternatively with 650- and 780-nm light. OA signals were detected with a cylindrically focused single-element transducer (V382-SU, 3.5 MHz, Olympus) followed by signal amplification by 60 dB with a wide-band voltage amplifier (DHPVA-100, Femto) and digitized at 100 MS/s with a data acquisition card (RZE-002 400, GaGe). Dependency of $P_{fr} \rightarrow P_r$ conversion on 770-nm pulse energy was measured with different pulse energies (0.4, 0.7, 1.0, and 1.3 mJ). Dependency of $P_{fr} \rightarrow P_r$ conversion on repetition rate of laser was measured with three different laser repetition rates (10, 25, and 50 Hz). Effect of different switching ON wavelength and resulting dynamic range at 770 nm was measured using different switching ON wavelength ranging from 630 to 680 nm.

SUPPLEMENTARY MATERIALS

Supplementary material for this article is available at http://advances.sciencemag.org/cgi/content/full/6/24/eaaz6293/DC1

View/request a protocol for this paper from *Bio-protocol*.

REFERENCES AND NOTES

1. V. Ntziachristos, D. Razansky, Molecular imaging by means of multispectral optoacoustic tomography (MSOT). *Chem. Rev.* **110**, 2783–2794 (2010).
2. L. V. Wang, S. Hu, Photoacoustic tomography: In vivo imaging from organelles to organs. *Science* **335**, 1458–1462 (2012).
3. P. Hai, T. Imai, S. Xu, R. Zhang, R. L. Aft, J. Zou, L. V. Wang, High-throughput, label-free, single-cell photoacoustic microscopy of intratumoral metabolic heterogeneity. *Nat. Biomed. Eng.* **3**, 381–391 (2019).
4. J. Yao, L. Wang, J.-M. Yang, K. I. Maslov, T. T. W. Wong, L. Li, C.-H. Huang, J. Zou, L. V. Wang, High-speed label-free functional photoacoustic microscopy of mouse brain in action. *Nat. Methods* **12**, 407–410 (2015).
5. J. Aguirre, M. Schwarz, N. Garzorz, M. Omar, A. Buehler, K. Eyerich, V. Ntziachristos, Precision assessment of label-free psoriasis biomarkers with ultra-broadband optoacoustic mesoscopy. *Nat. Biomed. Eng.* **1**, 68 (2017).
6. J. Reber, M. Willershäuser, A. Karlas, K. Paul-Yuan, G. Diot, D. Franz, T. Fromme, S. V. Ovsepian, N. Bézière, E. Dubikovskaya, D. C. Karampinos, C. Holzapfel, H. Hauner, M. Klingenspor, V. Ntziachristos, Non-invasive measurement of brown fat metabolism based on optoacoustic imaging of hemoglobin gradients. *Cell Metab.* **27**, 689–701.e4 (2018).
7. V. Gujrati, A. Mishra, V. Ntziachristos, Molecular imaging probes for multi-spectral optoacoustic tomography. *Chem. Commun.* **53**, 4653–4672 (2017).
8. J. Brunker, J. Yao, J. Laufer, S. E. Bohndiek, Photoacoustic imaging using genetically encoded reporters: A review. *J. Biomed. Opt.* **22**, 70901 (2017).
9. Y. Liu, P. Bhattarai, Z. Dai, X. Chen, Photothermal therapy and photoacoustic imaging: Via nanotheranostics in fighting cancer. *Chem. Soc. Rev.* **48**, 4950–4965 (2019).
10. C. Moore, J. V. Jokerst, Strategies for image-guided therapy, surgery, and drug delivery using photoacoustic imaging. *Theranostics* **9**, 1550–1571 (2019).
11. I. Steinberg, D. M. Huland, O. Vermesh, H. E. Frostig, W. S. Tummers, S. S. Gambhir, Photoacoustic clinical imaging. *Photoacoustics* **14**, 77–98 (2019).
12. F. Knieling, C. Neufert, A. Hartmann, J. Claussen, A. Urich, C. Egger, M. Vetter, S. Fischer, L. Pfeifer, A. Hagel, C. Kielisch, R. S. Görtz, D. Wildner, M. Engel, J. Röther, W. Uter, J. Siebler, R. Atreya, W. Rascher, D. Strobel, M. F. Neurath, M. J. Waldner, Multispectral optoacoustic tomography for assessment of crohn's disease activity. *N. Engl. J. Med.* **376**, 1292–1294 (2017).
13. L. V. Wang, J. Yao, A practical guide to photoacoustic tomography in the life sciences. *Nat. Methods* **13**, 627–638 (2016).
14. K. Mishra, J. P. Fuenzalida-Werner, V. Ntziachristos, A. C. Stiel, Photocontrollable proteins for optoacoustic imaging. *Anal. Chem.* **91**, 5470–5477 (2019).
15. A. C. Stiel, X. L. Deán-Ben, Y. Jiang, V. Ntziachristos, D. Razansky, G. G. Westmeyer, High-contrast imaging of reversibly switchable fluorescent proteins via temporally unmixed multispectral optoacoustic tomography. *Opt. Lett.* **40**, 367–370 (2015).
16. J. Yao, A. A. Kaberniuk, L. Li, D. M. Shcherbakova, R. Zhang, L. Wang, G. Li, V. V. Verkhusha, L. V. Wang, Multiscale photoacoustic tomography using reversibly switchable bacterial phytochrome as a near-infrared photochromic probe. *Nat. Methods* **13**, 67–73 (2016).
17. H. Dortay, J. Märk, A. Wagener, E. Zhang, C. Grötzinger, P. Hildebrandt, T. Friedrich, J. Laufer, Dual-wavelength photoacoustic imaging of a photoswitchable reporter protein, in *Photons Plus Ultrasound: Imaging and Sensing*, A. A. Oraevsky, L. V Wang, Eds. (International Society for Optics and Photonics, 2016), vol. 9708.
18. J. Märk, H. Dortay, A. Wagener, E. Zhang, J. Buchmann, C. Grötzinger, T. Friedrich, J. Laufer, Dual-wavelength 3D photoacoustic imaging of mammalian cells using a photoswitchable phytochrome reporter protein. *Commun. Phys.* **1**, 3 (2018).
19. L. Li, A. A. Shemetov, M. Baloban, P. Hu, L. Zhu, D. M. Shcherbakova, R. Zhang, J. Shi, J. Yao, L. V. Wang, V. V. Verkhusha, Small near-infrared photochromic protein for photoacoustic multi-contrast imaging and detection of protein interactions in vivo. *Nat. Commun.* **9**, 2734 (2018).
20. R. K. W. Chee, Y. Li, W. Zhang, R. E. Campbell, R. J. Zemp, In vivo photoacoustic difference-spectra imaging of bacteria using photoswitchable chromoproteins. *J. Biomed. Opt.* **23**, 106006 (2018).
21. D. M. Shcherbakova, M. Baloban, S. Pletnev, V. N. Malashkevich, H. Xiao, Z. Dauter, V. V. Verkhusha, Molecular basis of spectral diversity in near-infrared phytochrome-based fluorescent proteins. *Chem. Biol.* **22**, 1540–1551 (2015).
22. P. Vetschera, K. Mishra, J. P. Fuenzalida-Werner, A. Chmyrov, V. Ntziachristos, A. C. Stiel, Characterization of reversibly switchable fluorescent proteins in optoacoustic imaging. *Anal. Chem.* **90**, 10527–10535 (2018).
23. T. G. Dietterich, An experimental comparison of three methods for constructing ensembles of decision trees: Bagging, boosting, and randomization. *Mach. Learn.* **40**, 139–157 (2000).
24. S. Zhou, C. Gravekamp, D. Bermudes, K. Liu, Tumour-targeting bacteria engineered to fight cancer. *Nat. Rev. Cancer* **18**, 727–743 (2018).
25. L. Breiman, Random forests. *Mach. Learn.* **45**, 5–32 (2001).
26. J. E. Brown, L. Diaz, T. Christoff-Tempesta, K. M. Nesbitt, J. Reed-Betts, J. Sanchez, K. W. Davies, Characterization of nitrazine yellow as a photoacoustically active pH reporter molecule. *Anal. Chem.* **87**, 3623–3630 (2015).
27. D. Bellini, M. Z. Papiz, Structure of a bacteriophytochrome and light-stimulated protomer swapping with a gene repressor. *Structure* **20**, 1436–1446 (2012).
28. X. Yang, J. Kuk, K. Moffat, Crystal structure of *Pseudomonas aeruginosa* bacteriophytochrome: Photoconversion and signal transduction. *Proc. Natl. Acad. Sci. U.S.A.* **105**, 14715–14720 (2008).
29. J. R. Wagner, J. Zhang, D. von Stetten, M. Günther, D. H. Murgida, M. A. Mroginski, J. M. Walker, K. T. Forest, P. Hildebrandt, R. D. Vierstra, Mutational analysis *Deinococcus radiodurans* bacteriophytochrome reveals key amino acids necessary for the photochromicity and proton exchange cycle of phytochromes. *J. Biol. Chem.* **283**, 12212–12226 (2008).
30. C. J. C. Burges, A tutorial on support vector machines for pattern recognition. *Data Min. Knowl. Discov.* **2**, 121–167 (1998).
31. A. Liaw, M. Wiener, Classification and regression by randomForest. *R News* **2**, 18–22 (2002).
32. E. Osuna, R. Freund, F. Girosi, *Support Vector Machines: Training and Applications* (Massachusetts Institute of Technology, 1997).
33. X. Deán-Ben, A. Stiel, Y. Jiang, V. Ntziachristos, G. G. Westmeyer, D. Razansky, Light fluence estimation by imaging photoswitchable probes with temporally unmixed multispectral optoacoustic tomography, in *Optics InfoBase Conference Papers 3* (Optical Society of America, 2016).
34. L. V. Wang, H, Wu, *Biomedical Optics: Principles and Imaging* (Wiley-Interscience, 2007).

Acknowledgments: We thank A. Möglich for providing the wild-type BphPs, R. Hillermann for technical assistance, and A. C. Rodríguez for discussions on the manuscript. We further thank P. Vetschera for his initial contributions to the OA spectrometer device. **Funding:** K.M. and

A.C.S. received funding from DFG (STI656/1-1). V.R.B. received funding from DFG SFB 1054 (TP B09). Y.H. received funding from the China Scholarship Council via fellowship (CSC 201306960006). **Author contributions:** K.M. performed all measurements (for in vitro data with help from J.P.F.-W. and Y.H.; for in vivo measurements with assistance from U.K. and occasional help from V.G.). K.M. analyzed all in vitro data. All in vivo data were analyzed by M.S. along with K.M. M.S. wrote analysis code and GUI. S.G. established stable cell lines. A.C.S. wrote the manuscript and conceived the project together with K.M. and M.S. V.R.B. and V.N. contributed to the manuscript. **Competing interests:** V.N. is a shareholder of iThera Medical GmbH. All other authors declare no competing interests. **Data and materials availability:** Data availability: A reduced source data contents file is available online. Due to size limitations of depositing raw imaging data, the data that support the findings of this study are available from the corresponding author upon request. *Rp*BphP1-PCM, a derivative of the original *Rp*BphP1 from the laboratory of V. V. Verkhusha (Kaberniuk, Nat. Meth. 2016), can be provided by the authors' pending scientific review and a completed material transfer agreement to nonprofit organizations solely. Code availability: Detailed code is available from the corresponding author upon request. A version of the code meant for public use together with a GUI can be found at https://gitlab.lrz.de/ga45huk/rsoap_analysis/.

Submitted 26 September 2019
Accepted 1 May 2020
Published 12 June 2020
10.1126/sciadv.aaz6293

Citation: K. Mishra, M. Stankevych, J. P. Fuenzalida-Werner, S. Grassmann, V. Gujrati, Y. Huang, U. Klemm, V. R. Buchholz, V. Ntziachristos, A. C. Stiel, Multiplexed whole-animal imaging with reversibly switchable optoacoustic proteins. *Sci. Adv.* **6**, eaaz6293 (2020).

Science Advances

Multiplexed whole-animal imaging with reversibly switchable optoacoustic proteins

Kanuj Mishra, Mariia Stankevych, Juan Pablo Fuenzalida-Werner, Simon Grassmann, Vipul Gujrati, Yuanhui Huang, Uwe Klemm, Veit R. Buchholz, Vasilis Ntziachristos and Andre C. Stiel

Sci Adv **6** (24), eaaz6293.
DOI: 10.1126/sciadv.aaz6293